

# Evolution of Soot Particle Size Distribution Function in Burner-Stabilized Stagnation *n*-Dodecane–Oxygen–Argon Flames

Aamir D. Abid, Joaquin Camacho, David A. Sheen, and Hai Wang\*

Department of Aerospace and Mechanical Engineering, University of Southern California, Los Angeles, California 90089, USA

Received April 10, 2009. Revised Manuscript Received June 26, 2009

We investigate the evolution of particle size distribution of incipient soot formed in laminar premixed *n*-dodecane–oxygen–argon flames. The flames are established on a porous flat flame burner with equivalence ratio equal to 2 and a maximum flame temperature of 1800 and 1870 K. Detailed size distributions are obtained by the burner-stabilized stagnation (BSS) flame sampling approach using a scanning mobility particle sizer. The flame temperature profiles are determined for each separation distance between the burner surface and stagnation surface/probe orifice. It is shown that the flames can be modeled closely using an opposed jet flame code without having to estimate the effect of probe perturbation. The measured and simulated temperature profiles show good agreement. The evolution of the soot size distributions for *n*-dodecane flames are similar to those observed in ethylene flames. The size distributions are characteristically bimodal, indicating strong, persistent nucleation over a large range of residence times in the flame. Under similar conditions, the nucleation mode in the *n*-dodecane flames is stronger than that in comparable ethylene flames.

## Introduction

Basic understanding of the reaction kinetic process of jet-fuel combustion is a critical element toward optimal design of aviation gas-turbine engines. Soot formation is an integral part of this kinetic process. Because jet fuels contain a large number of compounds, and the composition may vary from batch to batch, a direct kinetic description of their combustion behaviors, including soot formation, is not feasible. A viable approach is to use a fuel surrogate, containing five to six pure compounds, to mimic jet-fuel behaviors.<sup>1</sup>

Typical jet-fuel surrogate mixtures contain mainly straight-chained, branched, and cyclic aliphatic hydrocarbons of which *n*-dodecane is an important *n*-alkane surrogate component.<sup>2</sup> In recent years, efforts have been directed at developing combustion reaction models for the surrogate fuel components.<sup>3–7</sup> At present, these models have been advanced

to explain global combustion behaviors, such as ignition delay times,<sup>8</sup> laminar flame speed,<sup>5,9,10</sup> and detailed time or spatial evolution of species concentrations resulting from fuel pyrolysis and oxidation in laboratory reactors.<sup>7,11</sup> We expect that these models will have to be extended to include soot chemistry, but reliable data for soot formation in *n*-dodecane flames do not exist.

Studies have shown that for a wide range of high-temperature combustion conditions, the oxidation kinetics of *n*-dodecane is governed, at least in part, by fuel cracking to smaller components (H<sub>2</sub>, CH<sub>4</sub>, C<sub>2</sub>H<sub>4</sub>, C<sub>3</sub>H<sub>6</sub>, etc.) followed by oxidation of cracked fragments.<sup>5,12–14</sup> Likewise, soot nucleation and growth in *n*-dodecane flames is expected to start from the reactions of cracked products. It is generally understood that the volume fraction of soot formed in laminar premixed flames is not particularly sensitive to fuel structure, since the fuel must undergo cracking before reaching the main flame zone; and soot forms behind the flame.<sup>15–19</sup> In other words, reactions and especially the process of soot formation have little to no memory of the parent fuel structure in premixed flames.

It is unclear, however, whether the detailed particle size distribution function (PSDF) is also insensitive to the fuel

\*To whom correspondence should be addressed. E-mail: haiw@usc.edu.

(1) Colket, M.; Edwards, J. T.; Williams, S.; Cernansky, N. P.; Miller, D. L.; Egolfopoulos, F. N.; Lindstedt, P.; Seshadri, K.; Dryer, F. L.; Law, C. K.; Friend, D. G.; Lenhart, D. B.; Pitsch, H.; Sarofim, A. F.; Smooke, M. D.; Tsang, W., Development of an Experimental Database and Kinetic Models for Surrogate Jet Fuels. In *45th AIAA Aerospace Sciences Meeting, Jan 8–11, Reno, NV, 2007*.

(2) Edwards, T. J. *Propul. Power* **2003**, *19*, 1089.

(3) Violi, A.; Yan, S.; Eddings, E. G.; Sarofim, A. F.; Granata, S.; Faravelli, T.; Ranzi, E. *Combust. Sci. Technol.* **2002**, *174*, 399.

(4) Ranzi, E.; Frassoldati, A.; Granata, S.; Faravelli, T. *Ind. Eng. Chem. Res.* **2005**, *44*, 5170.

(5) You, X.; Egolfopoulos, F. N.; Wang, H. *Proc. Combust. Inst.* **2009**, *32*, 403.

(6) Sirjean, B.; Dames, E.; Sheen, D. A.; You, X.; Sung, C. J.; Holley, A. T.; Egolfopoulos, F. N.; Wang, H.; Vasu, S. S.; Davidson, D. F.; Hanson, R. K.; Pitsch, H.; Bowman, C. T.; Kelley, A.; Law, C. K.; Tsang, W.; Cernansky, N. P.; Miller, D.; Violi, A.; Lindstedt, R. P. *A high-temperature chemical kinetic model of n-alkane oxidation, JetSurF, ver. 0.2*; URL: [http://melchior.usc.edu/JetSurF/Version0\\_2/Index.html](http://melchior.usc.edu/JetSurF/Version0_2/Index.html).

(7) Herbinet, O.; Marquaire, P. M.; Battin-Leclerc, F.; Fournet, R. *J. Anal. Appl. Pyrolysis* **2007**, *78*, 419.

(8) Vasu, S. S.; Davidson, D. F.; Hong, Z.; Vasudevan, V.; Hanson, R. K. *Proc. Combust. Inst.* **2009**, *32*, 173.

(9) Ji, C.; Dames, E.; Wang, Y. L.; Wang, H.; Egolfopoulos, F. N. *Combust. Flame* **2009**, DOI: 10.1016/j.combustflame.2009.06.011.

(10) Kumar, K.; Sung, C.-J. *Combust. Flame* **2007**, *151*, 209.

(11) Dahm, K. D.; Virk, P. S.; Bounaceur, R.; Battin-Leclerc, F.; Marquaire, P. M.; Fournet, R.; Daniau, E.; Bouchez, M. *J. Anal. Appl. Pyrolysis* **2004**, *71*, 865.

(12) Held, T. J.; Marchese, A. J.; Dryer, F. L. *Combust. Sci. Technol.* **1997**, *123*, 107.

(13) Zeppieri, S. P.; Klotz, S. D.; Dryer, F. L. *Proc. Combust. Inst.* **2000**, *28*, 1587.

(14) Seiser, H.; Pitsch, H.; Seshadri, K.; Pitz, W. J.; Curran, H. J. *Proc. Combust. Inst.* **2000**, *28*, 2029.

(15) Haynes, B. S.; Wagner, H. G. *Prog. Energy Combust. Sci.* **1981**, *7*, 229.

(16) Glassman, I. *Proc. Combust. Inst.* **1988**, *22*, 295.

(17) Frenklach, M.; Clary, D. W.; Gardiner, W. C., Jr; Stein, S. E. *Proc. Combust. Inst.* **1988**, *21*, 1067.

(18) Harris, S. J.; Weiner, A. M. *Proc. Combust. Inst.* **1985**, *20*, 969.

(19) Takahashi, F.; Glassman, I. *Combust. Sci. Technol.* **1984**, *37*, 1.

structure. Recent studies on ethylene and other flames have shown that bimodality is a ubiquitous feature of nascent soot size distribution.<sup>20–33</sup> The detailed features of the size distribution are sensitive to the flame temperature<sup>23</sup> and that these features are indicative of various competing, elementary processes of soot formation.<sup>26</sup> At present, it is unclear whether the various PSDF features observed for ethylene flames are applicable to *n*-dodecane flames.

Probe sampling in conjunction with a scanning mobility particle sizer (SMPS) has proved to be a useful tool in spatially resolving soot and other nanoparticle formation in flames.<sup>20–22,31,33–35</sup> This technique allows the investigation of soot formation from particle nucleation to mass growth. On the other hand, probe sampling is inherently intrusive to the flame. In a recent study,<sup>32</sup> we proposed a modified sampling approach in which the sample probe is also a stagnation surface that stagnates the burned gas flow downstream from the main flame zone of a burner-stabilized flame. The method, called burner-stabilized stagnation (BSS) flame approach, allows for intrusive soot sampling, but the probe perturbation can be captured quite rigorously as a boundary condition of the flame. The advantage of this technique is that the flame can be completely modeled using a quasi-one-dimensional opposed jet code.

The objective of this study is to provide an initial experimental database for soot formation in flames burning surrogate-fuel components using the BSS flame approach. This study investigates the evolution of size distribution of nascent soot formed in two *n*-dodecane flames, by varying the cold gas velocity to achieve flame temperature variations. A liquid fuel system was developed that allows for effective fuel vaporization before being mixed with the oxidizer and diluent. Detailed particle size distributions, number density, and volume fraction data are presented for each flame over a range of burner-to-stagnation surface separations. Additionally, numerical simulations were carried out using a recently proposed, detailed reaction model of *n*-alkane combustion<sup>6</sup> to examine the flame structure and conditions under which the PSDFs were probed. Temperature profiles are measured and compared to results of numerical simulations.

**Table 1. Summary of Flames Studied**

flame	mole fractions				equivalence ratio, $\phi$	velocity, $v_0$ (cm/s) <sup>a</sup>	maximum temperature, $T_f$ (K) <sup>b</sup>
	C <sub>12</sub> H <sub>26</sub>	O <sub>2</sub>	Ar	N <sub>2</sub>			
E1	0.025	0.229	0.670	0.076	2	4.94	1807
E2	0.025	0.229	0.689	0.057	2	6.58	1875

<sup>a</sup> Cold gas velocity at the STP condition. <sup>b</sup> Corrected for radiation heat loss.

## Experimental Methods

Details of the BSS flame approach are given elsewhere.<sup>32</sup> Two lightly sooting *n*-dodecane-oxygen-argon-nitrogen flames (Table 1) were stabilized at atmospheric pressure over a sintered porous plug with an outer diameter of 3 in. The flame was isolated from the ambient air by a shroud of nitrogen flowing at 43.6 cm/s (STP) through a concentric porous ring.

Soot was sampled on the centerline of the flame over several burner-to-stagnation surface distances with a positional accuracy of  $\pm 0.05$  cm. Since our first series of studies that used the SMPS technique, in which the potential particle losses were examined with caution and care,<sup>21,22</sup> the sampling technique has been improved further over the past few years, particularly with regard to particle losses in the sampling line.<sup>20,23,25,31,32</sup> Briefly, the sample probe is made of a stainless steel tube press-fit into a hole cut into a flat aluminum plate, which serves as a surface for flow stagnation and for sampling. The aluminum plate was water-cooled to maintain a constant temperature on the surface facing the incoming flame gas. A thin slit was cut into the bottom of the plate such that the sampling orifice in the stainless steel tube was exposed and was flush with the bottom of the plate. The plate was positioned parallel to the burner surface. The orifice was placed on the central axis of the burner. This sampling method creates a flame stabilized by heat loss to the burner surface, but the flow downstream diverges because of flow stagnation. For each burner-to-stagnation surface separation, the boundary conditions of this flame are defined, if the temperatures of the burner and stagnation surfaces are determined carefully, and the reactant composition and mass flow rates are known. As shown in an earlier study,<sup>32</sup> the flame is suitable for rigorous numerical simulation using a quasi-one-dimensional opposed jet or stagnation flame code and detailed reaction kinetics.

Temperature of the burner and stagnation plate was measured by type-K thermocouples. For the stagnation plate, the thermocouple was embedded at the bottom of the plate facing the incoming gas flow. Care was taken to position the thermocouple flush with the bottom of the plate so as to maintain a flat stagnation surface above the burner. For the burner temperature, the thermocouple was embedded at the bottom of the porous plug.

*n*-Dodecane was introduced to the reactant flow via a HPLC liquid pump (ChromTech Series III) with a maximum flow rate of 10 mL/min and  $\pm 2\%$  accuracy over the flow range. A nebulizer (Precision Glassblowing, Colorado USA) was used to aerosolize the liquid with mean droplet diameter of  $\sim 2 \mu\text{m}$ . The liquid was nebulized using a nitrogen flow at upstream pressure of 30 PSIG. At this pressure, the orifice in the nebulizer delivers a constant gas flow at 1 L/min (STP). The aerosol was introduced in a pyrex mixing/heating chamber where the atomized liquid is mixed with an oxygen/argon cross-flow as shown in Figure 1. The mixing chamber, the transfer line to the burner, and the burner itself was maintained at a temperature of 220 °C to prevent *n*-dodecane from condensing. Under this temperature and with a similar residence time in the reactant delivery line, no oxidation or fuel pyrolysis was observed in a similar experiment,<sup>9</sup> as confirmed by GC analyses of the unburned gas.

Unlike previous studies, the burner was not cooled. No trace of fuel condensation was seen inside the reactant delivery system. Also, the flame ignition and extinction response was

(20) Abid, A. D.; Tolmacheff, E. D.; Phares, D. J.; Wang, H.; Liu, Y.; Laskin, A. *Proc. Combust. Inst.* **2009**, *32*, 681.

(21) Zhao, B.; Yang, Z. W.; Wang, J. J.; Johnston, M. V.; Wang, H. *Aerosol Sci. Technol.* **2003**, *37*, 611.

(22) Zhao, B.; Yang, Z. W.; Johnston, M. V.; Wang, H.; Wexler, A. S.; Balthasar, M.; Kraft, M. *Combust. Flame* **2003**, *133*, 173.

(23) Zhao, B.; Yang, Z. W.; Li, Z. G.; Johnston, M. V.; Wang, H. *Proc. Combust. Inst.* **2005**, *30*, 1441.

(24) Oktem, B.; Tolocka, M. P.; Zhao, B.; Wang, H.; Johnston, M. V. *Combust. Flame* **2005**, *142*, 364.

(25) Zhao, B.; Uchikawa, K.; Wang, H. *Proc. Combust. Inst.* **2007**, *31*, 851.

(26) Singh, J.; Patterson, R. I. A.; Kraft, M.; Wang, H. *Combust. Flame* **2006**, *145*, 117.

(27) Maricq, M. M. *Combust. Flame* **2006**, *144*, 730.

(28) Manziello, S. L.; Lenhart, D. B.; Yozgatligil, A.; Donovan, M. T.; Mulholland, G. W.; Zachariah, M. R.; Tsang, W. *Proc. Combust. Inst.* **2007**, *31*, 675.

(29) Sgro, L. A.; Borghese, A.; Speranza, L.; Barone, A. C.; Minutolo, P.; Bruno, A.; D'Anna, A.; D'Alessio, A. *Environ. Sci. Technol.* **2008**, *42*, 859.

(30) Sgro, L. A.; Barone, A. C.; Commodo, M.; D'Alessio, A.; De Filippo, A.; Lanzuolo, G.; Minutolo, P. *Proc. Combust. Inst.* **2009**, *32*, 689.

(31) Abid, A. D.; Heinz, N.; Tolmacheff, E.; Phares, D.; Campbell, C.; Wang, H. *Combust. Flame* **2008**, *154*, 775.

(32) Abid, A. D.; Camacho, J.; Sheen, D. A.; Wang, H. *Combust. Flame* **2009**, doi 10.1016/j.combustflame.2009.05.010.

(33) Sgro, L. A.; De Filippo, A.; Lanzuolo, G.; D'Alessio, A. *Proc. Combust. Inst.* **2007**, *31*, 631.

(34) Maricq, M. M.; Harris, S. J.; Szente, J. J. *Combust. Flame* **2003**, *132*, 328.

(35) Thierley, M.; Grotheer, H.-H.; Aigner, M.; Yang, Z.; Abid, A.; Zhao, B.; Wang, H. *Proc. Combust. Inst.* **2007**, *31*, 639.

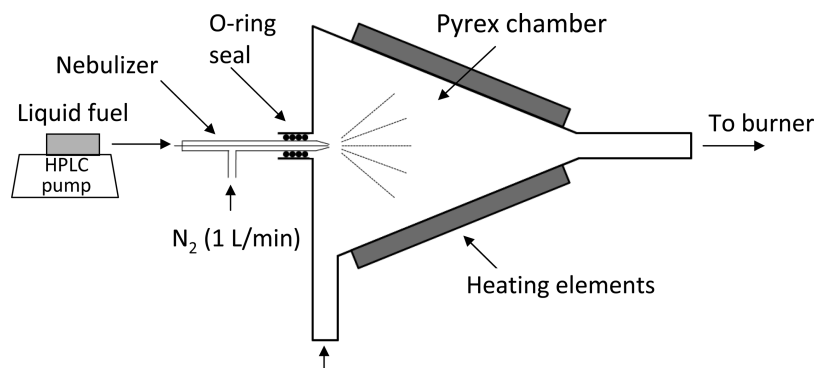


**Figure 1.** Schematic of liquid vaporization chamber.

approximately 3 s, close to the calculated residence time of the *n*-dodecane vapor in the delivery line, indicating that the fuel vapor stayed in the vapor phase throughout. The mass flow rates of oxygen, argon, and nitrogen were metered by critical orifices.

The reactant compositions are shown in Table 1. The equivalence ratio for both flames is kept constant at  $\phi=2$ . The maximum flame temperature was varied by adjusting the total cold gas velocity. In each experiment, the burner and the stagnation surface were allowed to reach steady-state temperatures, both of which are reported as a part of a detailed temperature profile. The gas temperature was determined using a type-S thermocouple coated with a Y/Be/O mixture to prevent surface catalysis. The diameter of the coated thermocouple wire was 125  $\mu\text{m}$ . The positional uncertainty of the thermocouple was  $\pm 0.03$  cm. Thermocouple radiation corrections were made using the procedure of Shaddix.<sup>36</sup> Uncertainty for the measured temperature was based largely on the uncertainty of the emissivity of the ceramic coating. Literature values for Y/Be/O ceramic coating ranges from 0.3 to 0.6.<sup>37</sup> The temperature reported is after correction for radiation heat loss and represents the mean value over that range of emissivity. The gas mixture properties were calculated iteratively by OPPDIF<sup>38</sup> using a detailed reaction model, JetSurF ver. 0.2.<sup>6</sup>

The flame sample entered the probe through the orifice and was immediately diluted with a cold nitrogen flow at 30 L/min. To ensure that particle losses were negligible in the sampling line, we used the particle dilution procedure identical to previous studies.<sup>21,22</sup> The dilution ratio was calibrated by measuring the CO concentration using a gas chromatograph.<sup>31,32</sup> Typical dilution ratio ranges from  $10^3$  to  $10^4$ . Visual observations of the soot accumulated over time on the sampling plate indicated that the soot from *n*-dodecane flames is “stickier” and more dense compared with soot produced from a similar ethylene flame,<sup>32</sup> possibly due to a lower extent of carbonization for the *n*-dodecane flame soot.

A standard SMPS system from TSI was used to classify the flame aerosols. The SMPS consists of a single-stage inertial impactor with an orifice diameter of 0.071 cm, a TSI 3077 charger, and a 3080 classifier with a nano-differential mobility analyzer (TSI 3085, nDMA) and a TSI 3025A ultrafine condensation particle counter (UCPC). The UCPC has a lower mobility size limit of 3 nm due to small activation efficiency at smaller sizes. The sample and sheath flows through the DMA were 1.5 and 15 L/min, respectively. Corrections for diffusion losses in the transfer lines and DMA were made for as a function of particle diameter using the TSI AIM software.

Mobility measurements can overestimate the true size of particles smaller than 10 nm because of inherent limitations of the

empirical Cunningham slip correction.<sup>39</sup> This correction does not account for (a) the transition from diffuse to specular scattering,<sup>40</sup> and (b) the van der Waals gas-particle interactions; both effects are expected to be important for particles below 10 nm in diameter.<sup>39</sup> A nanoparticle transport theory,<sup>39–41</sup> in which these effects are accounted for, gives a parameterized relation between the mobility diameter  $D_{p,\text{SMPS}}$  and true diameter  $D_p$  as follows:

$$\frac{D_p}{D_{p,\text{SMPS}}} = \tanh(1.4566 + 0.010892D_{p,\text{SMPS}}) \times \left(1.0721 - \frac{0.4925}{D_{p,\text{SMPS}}}\right) \quad (1)$$

In the above equation,  $D_{p,\text{SMPS}}$  has units of nm. All diameters presented hereafter are corrected according to the above equation. In a previous study,<sup>20</sup> we used atomic force microscopy to investigate morphology. The results showed that nascent soot formed in similar premixed flames were liquid-like. Hence, the particles are assumed to be droplet-like and spherical.

### Computational Method

The flame chemistry was simulated using JetSurF (version 0.2)<sup>6</sup> developed recently as the result of a multidisciplinary collaboration. This high-temperature kinetic model includes 194 species and 1459 reactions and was developed to predict the combustion properties of normal alkanes up to *n*-dodecane. The base model of  $\text{H}_2/\text{CO}/\text{C}_1\text{--C}_4$  combustion is the USC-Mech II (111 species, 784 reactions),<sup>42</sup> developed over the past decade through a series of kinetic modeling and ab initio studies.<sup>43–53</sup>

The stagnation flow used in these experiments has a separation-to-diameter ratio  $\ll 1$ , suitable for quasi-one-dimensional simulation using OPPDIF.<sup>38</sup> In an earlier study of similar

(40) Li, Z. G.; Wang, H. *Phys. Rev. E* **2003**, *68*, 061207.

(41) Li, Z. G.; Wang, H. *J. Aerosol. Sci.* **2006**, *37*, 111.

(42) Wang, H.; You, X.; Joshi, A. V.; Davis, S. G.; Laskin, A.; Egolfopoulos, F. N.; Law, C. K. *USC Mech Version II. High-Temperature Combustion Reaction Model of H<sub>2</sub>/CO/C<sub>1</sub>–C<sub>4</sub> Compounds*, 2007.

(43) Davis, S. G.; Law, C. K.; Wang, H. *Combust. Flame* **1999**, *119*, 375.

(44) Davis, S. G.; Law, C. K.; Wang, H. *J. Phys. Chem. A* **1999**, *103*, 5889.

(45) Laskin, A.; Wang, H. *Chem. Phys. Lett.* **1999**, *303*, 43.

(46) Laskin, A.; Wang, H.; Law, C. K. *Int. J. Chem. Kinet.* **2000**, *32*, 589.

(47) Qin, Z.; Lissianski, V.; Yang, H.; Gardiner, W. C., Jr.; Davis, S. G.; Wang, H. *Proc. Combust. Inst.* **2000**, *28*, 1663.

(48) Wang, H. *Int. J. Chem. Kinet.* **2001**, *33*, 698.

(49) Law, C. K.; Sung, C. J.; Wang, H.; Lu, T. F. *AIAA J.* **2003**, *41*, 1629.

(50) You, X. Q.; Wang, H.; Goos, E.; Sung, C. J.; Klippenstein, S. J. *J. Phys. Chem. A* **2007**, *111*, 4031.

(51) Davis, S. G.; Joshi, A. V.; Wang, H.; Egolfopoulos, F. *Proc. Combust. Inst.* **2005**, *30*, 1283.

(52) Joshi, A. V.; Wang, H. *Int. J. Chem. Kinet.* **2006**, *38*, 57.

(53) Sivaramakrishnan, R.; Comandini, A.; Tranter, R. S.; Brezinsky, K.; Davis, S. G.; Wang, H. *Proc. Combust. Inst.* **2007**, *31*, 429.

(36) Shaddix, C. R. In *Correcting Thermocouple Measurements for Radiation Loss: a Critical Review. Proceedings of the 33rd National Heat Transfer Conference*; Albuquerque, NM, August 13–19, 1999.

(37) Peterson, R. C.; Laurendeau, N. M. *Combust. Flame* **1985**, *60*, 279.

(38) Lutz, A. E.; Kee, R. J.; Grcar, J.; Rupley, F. M. *OPPDIF: A FORTRAN Program for Computing Opposed-Flow Diffusion Flames*; Sandia National Laboratories, Albuquerque, NM: 1996.

(39) Li, Z. G.; Wang, H. *Phys. Rev. E* **2003**, *68*, 061206.

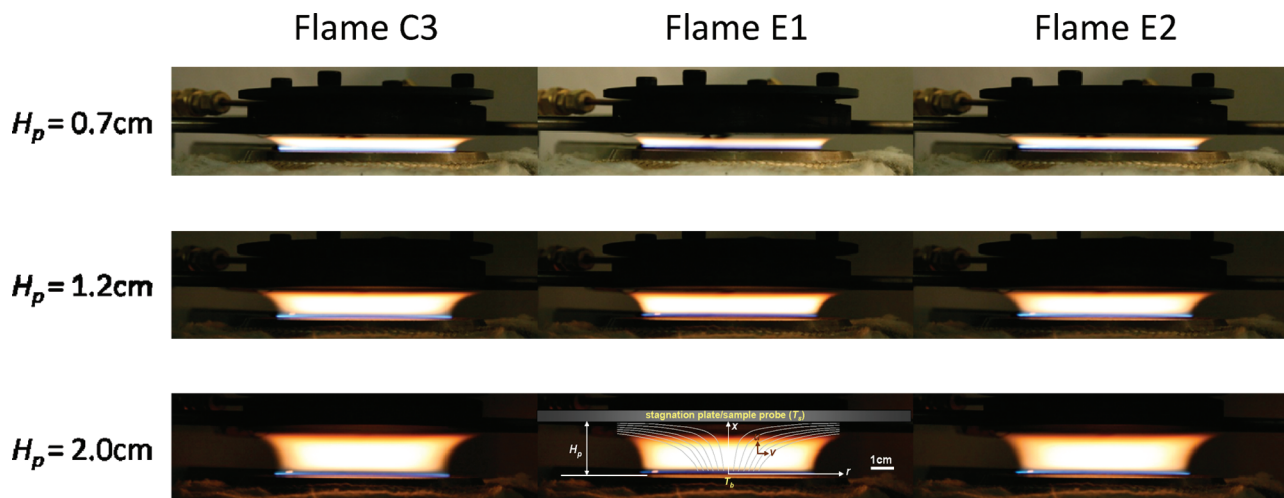


**Figure 2.** Visual images of the flames studied. Flame C3 is an 16.3% ethylene–23.7% oxygen–argon flame ( $\phi = 2.07$ ) at atmospheric pressure ( $T_{f,\max} = 1837$  K) and a cold gas velocity of 8 cm/s.<sup>32</sup> Conditions of flames E1 and E2 are provided in Table 1. In these images, the yellow luminosity is overaccentuated. The luminosity of the actual flame is much lower than shown.

ethylene flames, we showed that the numerical formulation implemented can account for entire temperature profiles in the flame for all burner-to-stagnation surface separations studied.<sup>32</sup> The advantage of this combined experimental and computational method is clear, in that the boundary conditions are well-defined and the inherent flame perturbation due to probe sampling can be accounted for quantitatively.

The lower, middle panel of Figure 2 depicts the coordinate system and the flow velocity components of the flames simulated. Boundary conditions are defined as follows. At the burner exit, defined as  $x = 0$ , the flow is a uniform plug flow with fixed mass flux and temperature equal to the measured burner temperature  $T_b$ . Each species has an inlet mass fraction defined as  $Y_{k,0}$ , and the boundary condition is constructed so that the mass flux of each species is  $\dot{m}_0 Y_{k,0}$ . These flow boundary conditions can be expressed as

$$F = \rho u/2 = \dot{m}_0/2 \quad (2)$$

$$G = \rho v/r = 0 \quad (3)$$

$$\rho Y_k(u + V_k) = \dot{m}_0 Y_{k,0} \quad (4)$$

where  $\rho$  is the mass density;  $u$  and  $v$  are the axial and radial convective velocities, respectively;  $r$  is the radial coordinate; and  $V_k$  is the axial diffusion velocity of species  $k$ . The plate, located at  $x = H_p$ , is treated as a no-slip wall; so  $u$ ,  $v$ , and  $V_k$  are all 0; and it has a fixed temperature  $T_s$  equal to the measured plate temperature.

The simulation used windward differencing, multicomponent transport, and thermal diffusion. Heat release rates and transport properties were solved using Sandia CHEMKIN<sup>54</sup> and TRANSPORT.<sup>55</sup> Adaptive mesh resolution was used, and it was found that the flame is sufficiently resolved with roughly 200 points. Radiation correction was carried out as discussed in detail by Egolfopoulos<sup>56</sup> and described in Abid et al.<sup>32</sup> The radiation heat loss due to soot in these lightly sooting flames is negligible, as confirmed by simulations using roughly the soot volume fraction

measured. The computed results reported herein are those with radiation loss by gas phase species only.

## Results and Discussion

Images of the flames studied (E1 and E2) are presented in Figure 2 for three burner-to-stagnation separations  $H_p = 0.7$ , 1.2, and 2.0 cm. In these images, the yellow luminosity is overaccentuated. In fact, the luminosity of the actual flame is much lower than shown. Visually, these *n*-dodecane flames do not differ from an ethylene flame (C3) observed previously,<sup>32</sup> as seen in the figure. In all cases, the burner issues an unburned gas, which travels upward toward the stagnation surface. Flow diverges toward the stagnation surface. As discussed earlier, the sample probe is located on the stagnation surface along the center axis of the flame. Each burner-to-stagnation separation yields a different flame because of different degrees of flow divergence and heat loss into the stagnation surface. Hence, the temperature profile must be measured for each  $H_p$  values, as will be reported below.

Temperature profiles are reported in Figure 3. As seen, both flames show similar trends of a sharp temperature gradient just above the burner surface, unaffected by the presence of the stagnation surface. Because of a lower unburned gas mass flux, the maximum flame temperature for flame E1 is lower than that of flame E2 by about 70 K. In all cases, the temperature drops to that of the stagnation surface, essentially quenching high-temperature chemical reactions a few millimeters downstream from the reaction zone.

The shape of these temperature profiles are captured very well by the simulation results, as shown in Figure 3. The  $x$ -error bars on the measurements ( $\pm 0.03$  cm) represent the uncertainties due to finite thermocouple bead diameter and micrometer positioning. The  $y$ -error bars shown are based on the uncertainty due to the wire emissivity. As seen, the simulated maximum temperature predicts the measurements well, except the preheat region where the measured temperatures are somewhat lower than model predictions. Toward greater distances from the burner surface, the simulated temperature is again larger than the experimental value, and in some cases, over 100 K. These discrepancies could be caused by thermocouple positional uncertainty, since the fine wire is bent slightly by the convective flow and the degree to which it

(54) Kee, R. J.; Rupley, F. M.; Miller, J. A. *CHEMKIN-II: A FORTRAN Chemical Kinetics Package for the Analysis of Gas-Phase Chemical Kinetics*, SAND89–8009; Sandia National Laboratories: Albuquerque, NM, 1989.

(55) Kee, R. J.; Dixon-Lewis, G.; Warnatz, J.; Coltrin, M. E.; Miller, J. A. *A FORTRAN Computer Code Package for the Evaluation of Gas-Phase Viscosities, Conductivities, and Diffusion Coefficients*, SAND86–8246; Sandia National Laboratories: Albuquerque, NM, 1986.

(56) Egolfopoulos, F. N. *Proc. Combust. Inst.* **1994**, *25*, 1375.

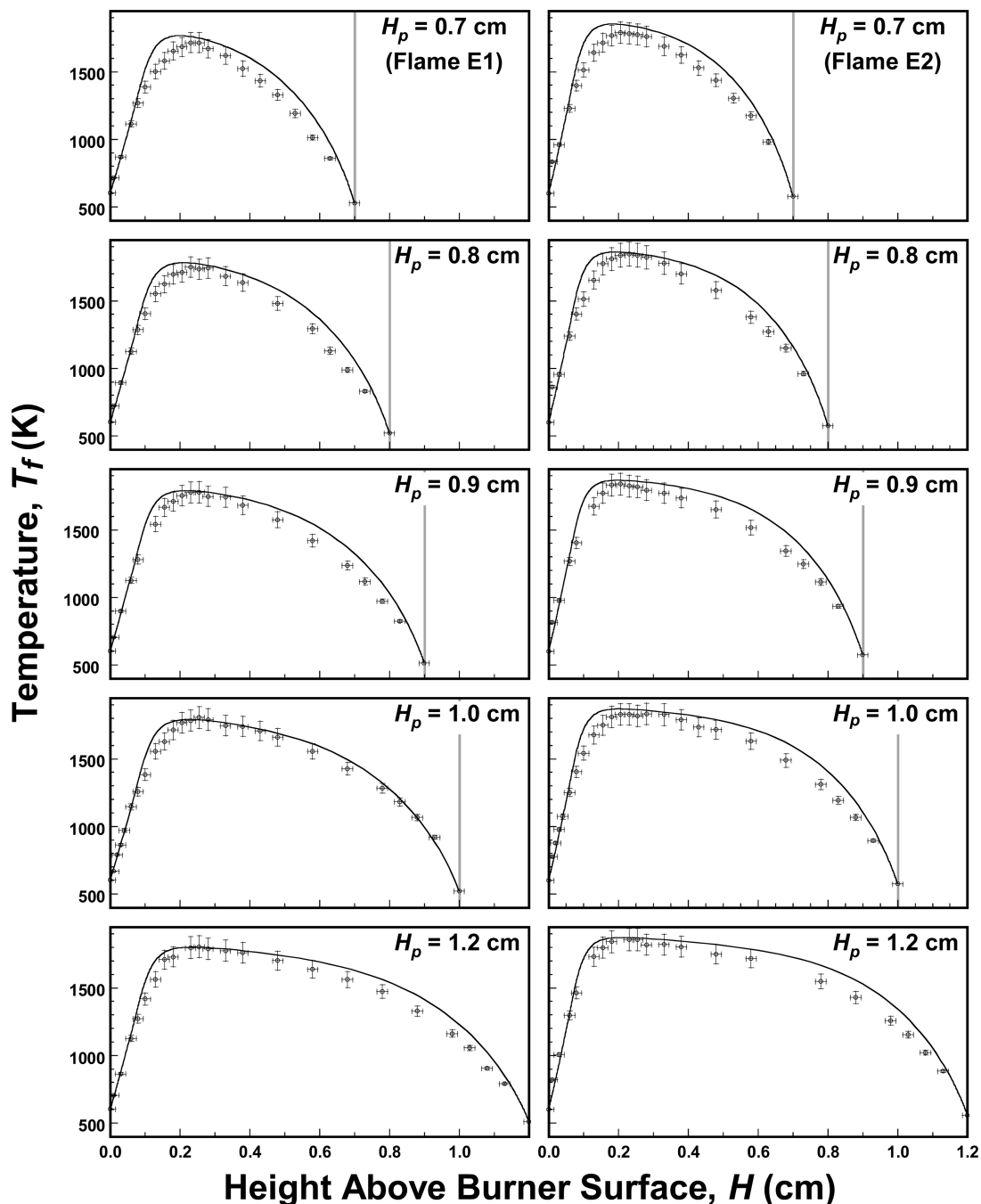


**Figure 3.** Comparison of measured (symbols, radiation corrected) and simulated (lines) temperature profiles at selected burner-to-stagnation surface separations. Left column shows data for flame E1 and right column shows data for flame E2.

bends is sensitive to the local flow velocity. In the preheat region, the larger predicted temperature could also be caused by uncertainties in JetSurF. We note that this is the first time this reaction model is being compared to combustion observations under fuel-rich sooting conditions. Nonetheless, the overall agreement shown in Figure 3 is encouraging, keeping in mind that only the boundary temperatures, the reactant composition, and mass flux were used as input parameters in the numerical simulations.

An important aspect of the BSS flame approach is that the temperature profile is solved directly by energy conservation without having to impose measured temperature as an input to the solution of the species conservation equations. Comparisons of the experimental and computed temperature

profiles yield information more critical to the characteristics of local heat release and heat loss rates. These rates determine the local temperature, which, in turn, dictates the species concentrations through Arrhenius reaction kinetics and species transport. For these reasons, while comparisons of species concentrations are useful, they are of secondary importance, since these comparisons are, to a greater extent, subject to reaction model uncertainties.

To understand the effect of the boundary conditions on the flame response, a sensitivity analysis was performed by perturbing (a) the cold gas velocity, (b) the temperature of the burner exit, and (c) stagnation plate for flame E1 with  $H_p = 1.2$  cm, as shown in Figure 4. Panel (a) shows a deviation of maximum flame temperature  $H_p$  by  $\sim 100$  K from the base

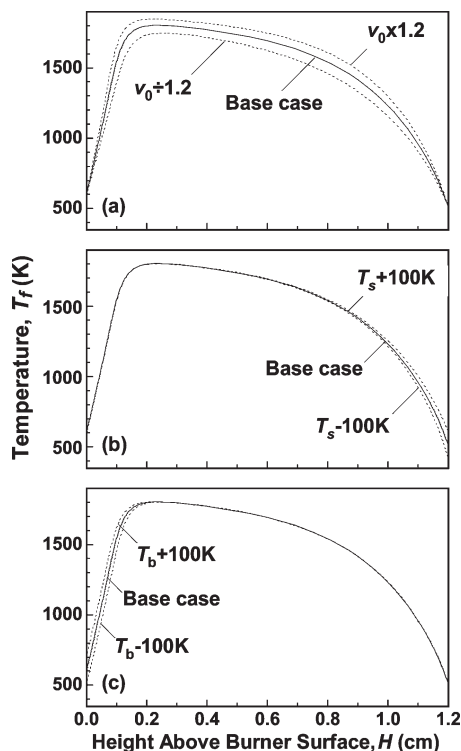


**Figure 4.** Computational sensitivity analysis for flame E1 with  $H_p = 1.2$  cm by perturbing (a) the mass flux, (b) the stagnation plate temperature  $T_s$ , and (c) the burner exit temperature  $T_b$ .

case when the mass flux is perturbed by 20%. Note that the extent of the perturbation is substantially larger than the uncertainty of our flow measurements, which is around 2%. Additionally, perturbing the burner exit temperature and the plate temperature by 100 K (again, substantially larger than the uncertainty of our temperature measurements) has small effects on the entire temperature profile. Two conclusions may be drawn from these numerical analyses. First, with the experimental setup the flame is not affected by perturbations of the boundary conditions significantly. Second, the discrepancies seen in Figure 3 are probably not caused by uncertainties in the flame boundary conditions.

The major and minor species profiles computed for flame E1 at the  $H_p$  value of 1.2 cm are shown in Figures 5 and 6, respectively. These profiles are typical for fuel-rich flames and are qualitatively similar for all  $H_p$  values studied. For major species, all of the mole fraction profiles computed are nearly constant in the post flames, with the exception of  $H_2$ . Computationally, the use of a stagnation surface causes the  $H_2$  mole fraction to undergo notable changes toward the stagnation surface. All of the free radical concentrations also drop rapidly, as shown in Figure 6.

The fact that the axial convective velocity vanishes at  $x = H_p$  states that the diffusive flux is equal to that of chemical source term for each species immediately adjacent to the stagnation surface. The species concentrations at the stagnation surface are dictated by the balance of the diffusive velocities and chemical reactions. Thus, although the “residence” time of a fluid particle is infinite at the stagnation surface, that of a particular chemical species is not. These balances cause drastic changes in the concentrations of species adjacent to the surface, especially for species with molecular weight far different from the mean molecular weight of gas.

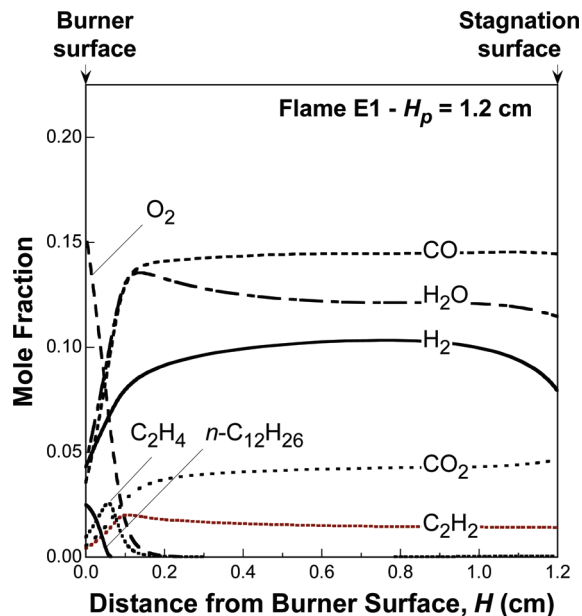


**Figure 5.** Mole fraction profiles of major species computed for flame E1 with  $H_p = 1.2$  cm.

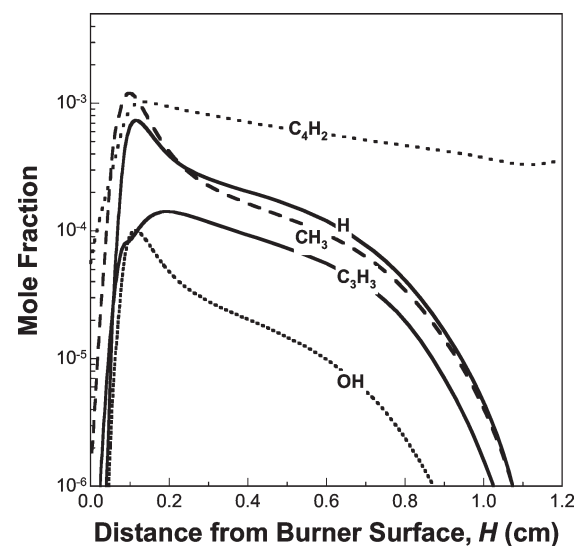


**Figure 6.** Mole fraction profiles of selected minor species computed for flame E1 with  $H_p = 1.2$  cm.

What is perhaps more interesting is the benzene mole fraction profiles computed for these flames. Figure 7 shows that the presence of the stagnation surface causes the benzene mole fractions to vary widely as a function of  $H_p$ . This variation is certainly caused by both temperature and local flow velocity. Toward the stagnation surface, benzene concentration undergoes a rapid rise, again because of cooling and reduced rates of fragmentation. It is worth noting that had benzene concentrations been measured at the stagnation surface (or by a probe) its concentration would exhibit an apparent increase in the post flame of E1, and it would be opposite for flame E2. This behavior has been discussed earlier<sup>57</sup> and can be attributed to the influence of flame temperature on the competition between molecular weight growth and fragmentation. In any case, in our earlier studies

(57) Wang, H.; Frenklach, M. *Combust. Flame* 1997, 110, 173.

of ethylene flames under comparable conditions, we demonstrated that if the concentration of soot precursors, that is, the aromatics, does not decay or decays mildly in the postflame regime, the soot size distribution would be bimodal. The cause for the bimodality is the persistent particle nucleation that competes with particle size growth by coagulation.<sup>22,23</sup>

Indeed the PSDFs measured for both *n*-dodecane flames are bimodal, as shown in Figures 8 and 9 for flames E1 and E2, respectively. In these figures, the different symbols designate multiple runs and the overlap of symbols shows that the data are reproducible. For the lower temperature flame (E1) with  $T_{f,max} = 1807$  K, the transition to bimodality occurs at higher  $H_p$  values than that for flame

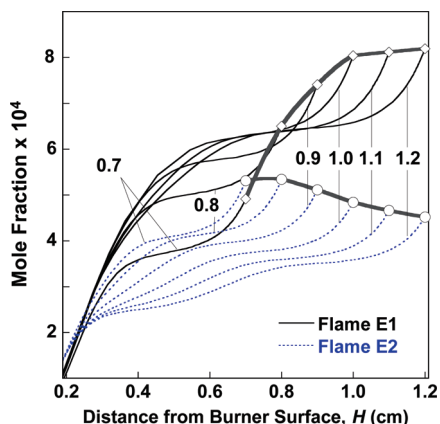


**Figure 7.** Benzene mole fraction profiles (thin lines) computed for flames E1 and E2 at selected  $H_p$  values. Symbols and thick lines indicate the benzene mole fraction at the stagnation (sampling) surface.

E2, as expected because of a larger standoff distance of the reaction zone. Like the ethylene flames, these PSDFs can be described by a bilognormal distribution, as shown by the lines of Figures 8 and 9,

$$\frac{dN}{d \log D_p} = \sum_{i=1}^2 \frac{N_i}{\sqrt{2\pi} \log \sigma_i} \exp\left\{-\frac{[\log(D_p/\langle D_p \rangle_i)]^2}{2(\log \sigma_i)^2}\right\} \quad (5)$$

where  $\sigma_i$  is the geometric standard deviation of the *i*th mode, and  $\langle D_p \rangle_i$  is the median diameter of that mode. Mode 1 corresponds to the nucleation mode, and mode 2 is the growth mode. Although many of the features are qualitatively the same, quantitatively the fine details of the PSDFs are indicative of the competition of various elementary particle processes.<sup>26</sup>

For flame E1,  $T_{f,max} = 1807$  K, and for flame E2,  $T_{f,max} = 1875$  K. Two important differences emerge as we compare the PSDFs of the two flames as Figure 10 shows: the lower temperature flame has larger median particle diameters for the growth mode, as seen by the difference in  $\langle D_p \rangle_2$  values; and the transition from mode 1 to mode 2 occurs at larger particle size, as shown by the difference in  $D_{p,t}$  values. The difference in the median particle diameter is consistent with the concentrations of benzene computed for the two flames. As shown in Figure 7, the benzene mole fraction of flame E1 is notably larger than that of flame E2.

In flame E1, the larger values measured for the diameter at the trough  $D_{p,t}$  is accompanied by somewhat greater intensities of the nucleation mode. This can be attributed to a greater extent of increase in the precursor concentration as predicted for benzene. Although benzene is not likely to be the nucleating species, its spatial variation is indicative of

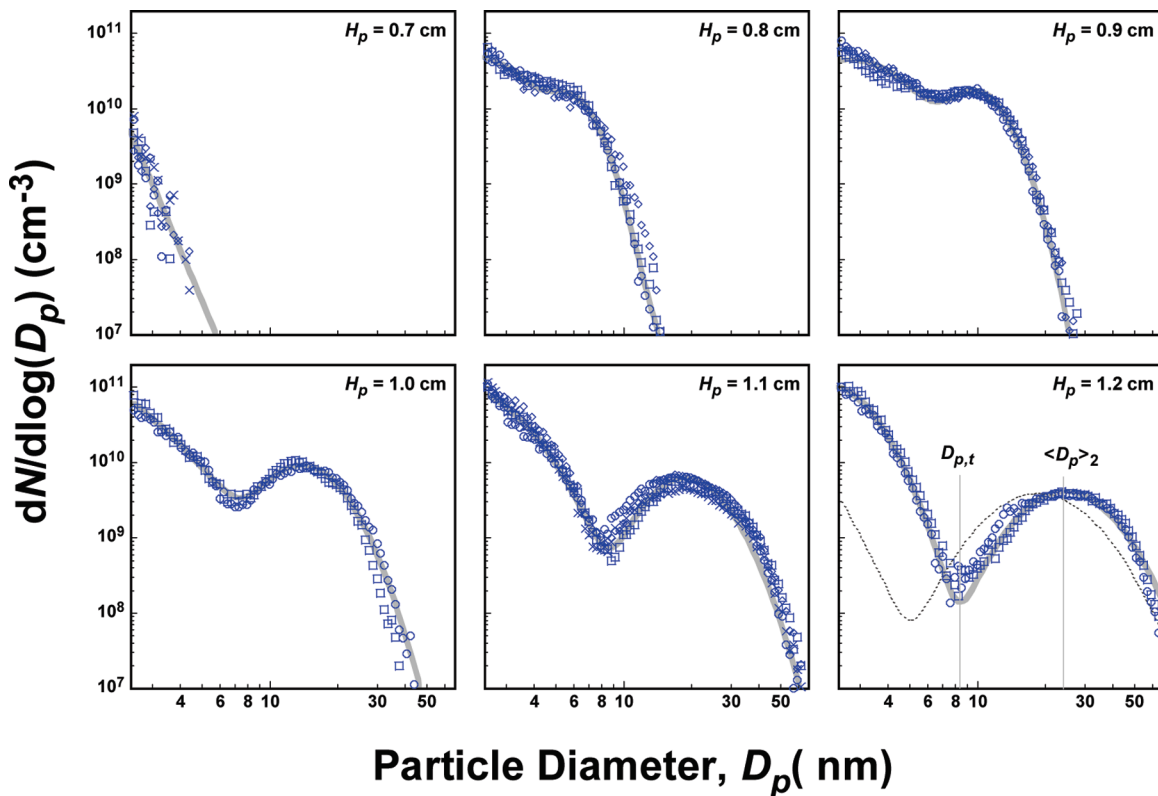


**Figure 8.** Evolution of particle size distribution functions at increasing burner-to-stagnation surface separations for flame E1. Symbols are experimental data; lines are bi-lognormal fits to data. The dashed line plotted for  $H_p = 1.2$  cm is taken from ref 32, measured for a comparable ethylene flame (C3) with  $T_{f,max} = 1837$  K.

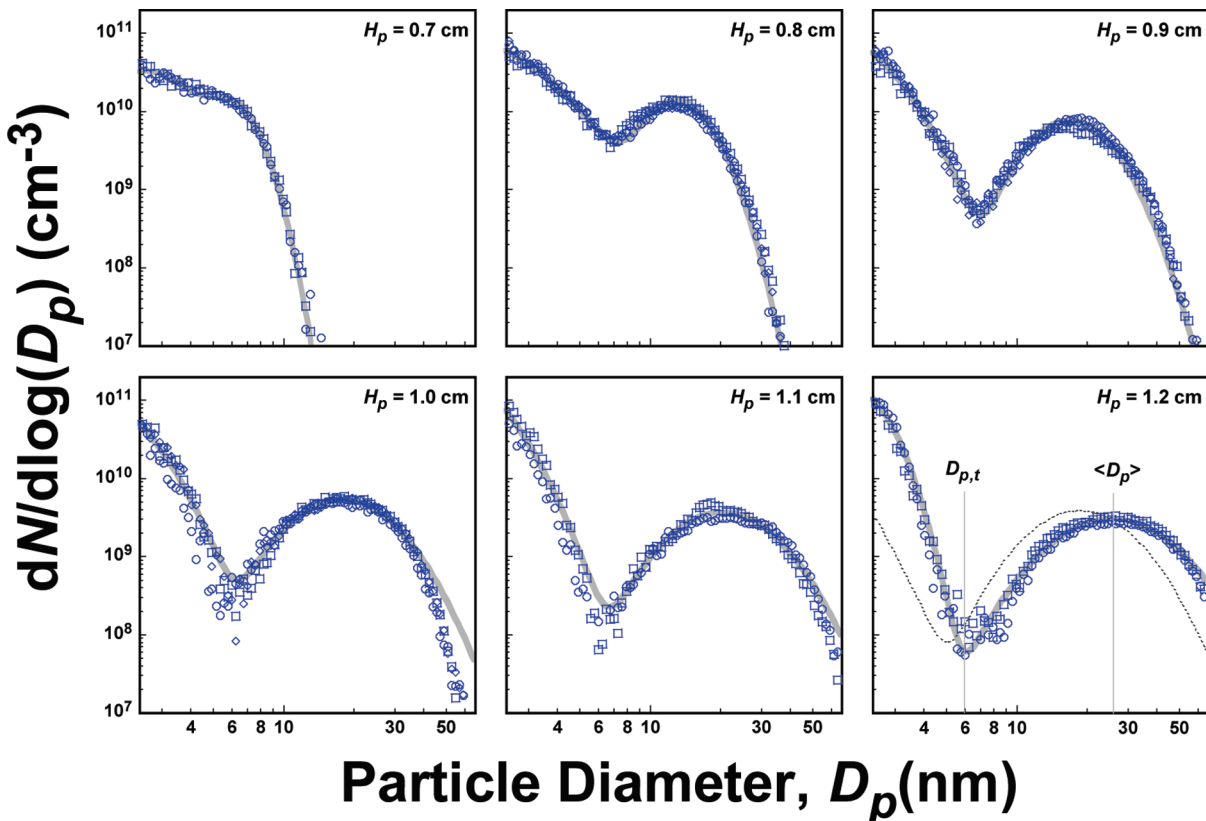


**Figure 9.** Evolution of particle size distribution functions at increasing burner-to-stagnation surface separation for flame E2. Symbols are experimental data; lines are bi-lognormal fits to data. The dashed line plotted for  $H_p = 1.2$  cm is taken from ref 32, measured for a comparable ethylene flame (C3) with  $T_{f,\max} = 1837$  K.

the variations of larger, polycondensed aromatics.<sup>57</sup> Numerical sensitivity analysis reported by Singh et al.<sup>26</sup> on the shape of these bimodal distributions indicates that the position of the trough is strongly influenced by the nucleation rate and the size of the nuclei. In addition, a longer residence time in flame E1 can also contribute to the increased nucleation mode intensity. Considering the separation distance of  $H_p = 1.2$  cm, the residence time for a parcel of fluid exiting the burner to reaching 0.1 cm below the stagnation surface is  $\sim 70$  ms for flame E1 and  $\sim 50$  ms for flame E2. The longer residence time allows for prolonged nucleation resulting in a stronger nucleation tail for flame E1. Meanwhile the coagulation of the particles in the growth mode becomes increasingly insignificant as it is indicative by their number densities dropping well below that of the particles of the nucleation mode.

For both flames, the nucleation modes appear to be stronger than that in a comparable ethylene flame ( $T_{f,\max} = 1736$  K) as shown for  $H_p = 1.2$  cm in Figures 8 and 9, indicating that the nucleation strength in these *n*-dodecane flames is stronger in the postflame region than the comparable ethylene flame. This difference cannot be attributed entirely to the somewhat shorter residence time, around 40 ms, for flame C3, in comparison with 70 and 50 ms in flames E1 and E2, respectively. Rather, the detailed flame characteristics must play a role in the differences observed for the nucleation strength.

It is worth noting that the soot sampled by the current technique is influenced by a thermophoretic velocity toward the stagnation surface<sup>32</sup> and a finite rate at which the sample probe withdraws the gas sample into the probe. The

thermophoretic velocity is well-defined and can be considered rigorously in numerical modeling. The sample withdrawal rate is difficult to quantify, as in all probe sample methods. We estimate that under typical probe operating conditions the soot sample must have been drawn into the probe from a volume adjacent to the orifice. This volume is equivalent to a cylinder roughly 0.06 cm in both height and diameter.<sup>32</sup> Hence, it is possible that the soot sampled represents an average of the flame gas next to the stagnation surface, yet viscous dissipation would dampen the suction very rapidly.

The volume fraction and particle number density may be derived from the PSDF data,

$$F_v = \int_{-\infty}^{\infty} \frac{\pi D_p^3}{6} \left( \frac{dN}{d \log D_p} \right) d \log D_p \quad (6)$$

$$N = \int_{-\infty}^{\infty} \left( \frac{dN}{d \log D_p} \right) d \log D_p \quad (7)$$

The results of both flames are shown in Figures 11 and 12, respectively. For volume fraction, we also include the results for a similar ethylene flame (flame C3).<sup>32</sup> Clearly, the evolution of the volume fraction and particle number density is similar to that seen in the ethylene flame. The final volume fraction for both *n*-dodecane flames is around  $10^{-8}$ , which is nearly identical to that of the ethylene flame. This observation is consistent with conclusion reached earlier<sup>15–19</sup> that the final soot volume fraction in premixed flat flames is not sensitive to the fuel structure. The number density of soot in both flames E1 and E2 is around  $10^{10}$  cm<sup>-3</sup>. Again, the constant number

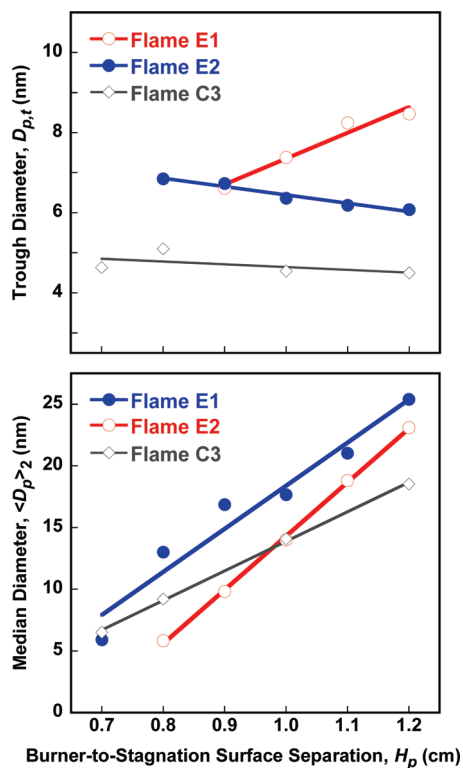


**Figure 10.** Particle diameter at the trough and median diameters of the growth mode of the soot PSDs obtained from bilognormal curve fits. Data for flame C3 is from ref 32. Symbols are experimental data; lines are drawn to guide the eye.

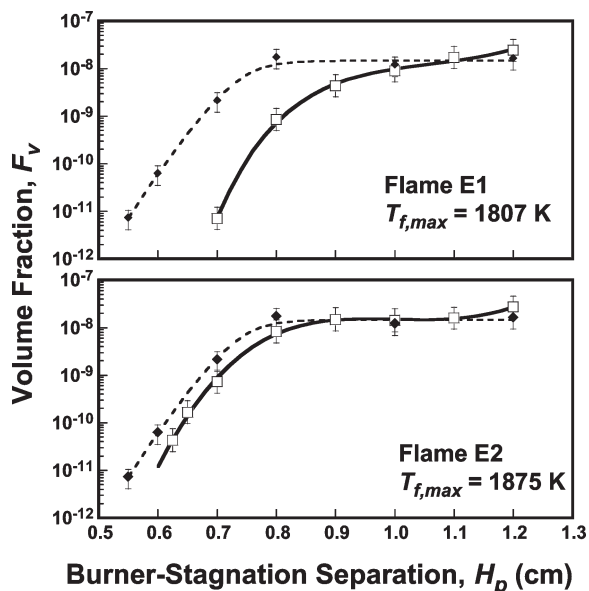


**Figure 11.** Soot volume fraction (open symbols) observed for  $D_p > 2.5$  nm in flames E1 and E2. Data for a comparable ethylene flame (C3, filled symbols) are also included. Lines are drawn to guide the eye.

density observed for flame E1 but a decreased number density in flame E2 at larger burner-to-stagnation surface separations are consistent with differences observed for the nucleation strengths between the two flames. To provide further insights into the observations made here, detailed kinetic modeling of

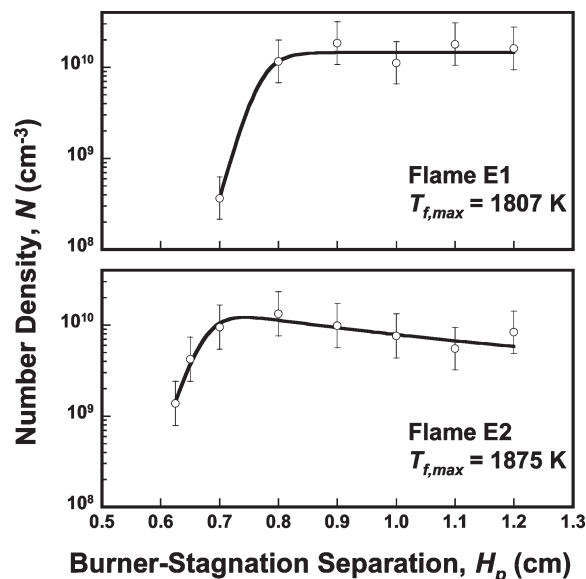


**Figure 12.** Number density profiles observed for  $D_p > 2.5$  nm in flames E1 and E2. Symbols are experimental data; lines are drawn to guide the eye.

soot formation is clearly necessary. In addition, comparisons of the major and minor species concentration profiles are desirable. These are, however, beyond the scope of the current study, since the reaction model for sooting *n*-dodecane flames is still under development, and measurements of the species concentrations for BSS flames are underway.

## Conclusions

Detailed particle size distribution, temperature, volume fraction, and number density data were measured for two premixed *n*-dodecane–oxygen–argon flames at equivalence ratio  $\phi = 2$  and atmospheric pressure in a burner-stabilized stagnation flow setup. The experimental temperature profiles are compared to simulations using the OPPDIF flame code. The experimental and computational results compare well with each other. The qualitative feature of the particle size distributions observed for the two flames, including the persistent bimodality, is similar to earlier observations made for comparable ethylene flames, again, indicating the insensitivity of soot formation to detailed fuel structure in premixed flames. The fine, quantitative feature of the soot PSDs in the *n*-dodecane flames can be different from that in an ethylene flame under comparable conditions. For example, the PSDs of the *n*-dodecane flames exhibit stronger nucleation intensities in the post flame region. The trough of the bimodal distributions in the *n*-dodecane flames occurs at larger particle size than that of the ethylene flame.

With the ability to quantify the flame boundary condition and eliminate the unquantifiable probe perturbation to the flame, the flame structure and species profiles can be predicted with a high level of confidence. Hence, these data provide a reliable experimental database to model soot formation from flames of real-fuel surrogate components.

**Acknowledgment.** This work was supported by the Strategic Environmental Research and Developmental Program and by the National Science Foundation (CBET 0651990).